

Cross-Channel Correlation Preserved Three-Stream Lightweight CNNs for Demosaicking

Yan Niu ^{*1} Jihong Ouyang ¹

Abstract

Demosacking is a procedure to reconstruct full RGB images from Color Filter Array (CFA) samples, none of which has all color components available. Recent deep Convolutional Neural Networks (CNN) based models have obtained state of the art accuracy on benchmark datasets. However, due to the sequential feature extraction manner of CNNs, deep demosaicking models may be over slow for daily use cameras. In this paper, we decouple deep sequential demosaicking to three-stream lightweight networks, which restore the green channel, the green-red difference plane and the green-blue difference plane respectively. This strategy allows independent offline training and parallel online estimation, whilst preserving the intrinsic cross-channel correlation of natural images. Moreover, this allows designing each stream according to the various restoration difficulty of each channel. As validated by extensive experiments, our method achieves top accuracy at fast speed. Source code will be released along with paper publication.

1. Introduction

Daily-use non-professional digital cameras mostly use Color Filter Arrays (CFA), which transduce the incident light at each pixel to one of the RGB intensity values. Most popularly, the CFAs are arranged according to the Bayer pattern: in each 2×2 block of pixels, the diagonal or anti-diagonal positions have their green intensity components captured, while the other two positions have their red and blue intensity components captured. The particular layouts are shown in Fig.1. Consequently, CFA cameras rely on a demosaicking procedure to restore the full RGB channels.



Figure 1. The four layouts of the Bayer pattern CFA.

It seems that demosaicking could be solved by simply applying monochrome Single Image Super-Resolution (SISR) techniques to each channel. However, demosaicking is beyond $2 \times$ SISR (Szeliski, 2010). In a CFA image, each channel is sampled at different pixel locations, consequently a small demosaicking bias in one color component may result in obvious “false color” or “zippering” artifacts. To address these issues, demosaicking *has to* handle cross-channel regularization more carefully than SISR. In this sense, demosaicking techniques not only benefits the camera industry, but also provide solutions to applications that infer image structure from data sparsely sampled in both the color and spatial dimensions.

A myriad of classical mathematical tools have been utilized to detect image structure from CFA images. For example, first- and second- order directional differencing (e.g., (Hamilton Jr. & Adams, 1997);(Malvar et al., 2004);(Pekkucuksen & Altunbasak, 2013)), variance of intensity variation (e.g., (Chung & Chan, 2006)), patch matching (e.g., (Buades et al., 2009)), contour stencils (e.g., (Getreuer, 2012)), non-local regularization (e.g.,(Menon & Calvagno, 2008); (Zhang et al., 2011); (Condat & Mosaddegh, 2012)), Maximum a Posterior estimation (e.g.,(Wu & Zhang, 2004); (Menon et al., 2007)), dictionary learning (e.g.,(Wu et al., 2016)), compressive representation ((Moghadam et al., 2010); (Rossi & Calvagno, 2014)) etc. The interpolation may be performed in the color planes (e.g., (Malvar et al., 2004)), the color difference planes (e.g., (Hamilton Jr. & Adams, 1997)), the residual planes (e.g., (Kiku et al., 2013); (Monno et al., 2015); (Kiku et al., 2016)), or the spectral domains (e.g.,(Tsai & Song, 2007); (Duran & Buades, 2014)). Due to the inherent cross-channel correlation in natural images, iteratively refining each channel by the other intermediately recovered channels can further improve the accuracy (e.g.,(Li, 2005); (Su, 2006); (Lu et al., 2010); (Kiku et al., 2016)). Among demosaicking schemes designed for the Bayer pattern, Hamilton-Adams (HA) algorithm (Hamilton Jr. & Adams, 1997) and Malvar-He-Cutler’s High Quality Linear Interpolation (HQLI) (Malvar et al., 2004) are two simplest yet effective approaches. To accomplish efficiency, this work adopts the cross-channel regularization principles of HA and

initializes the demosaicking process by HQLI.

In recent couple of years, residual Convolutional Neural Networks (CNN) for demosaicking have attracted intense attention. Wang applied a 3-layer neural network to demosaicking, learning the weights and bias parameters by a combination of supervised and unsupervised learning (Wang, 2014). Gharbi et al. designed a deep CNN structure with 15 convolution layers for jointly demosaicking and denoising, increasing demosaicking accuracy on benchmark datasets (Gharbi et al., 2016) to a new level. Tan-Chen-Hua trained three deep CNNs for general images, smooth textures and rough textures respectively, fusing the outputs at the final stage by weighted interpolation (Tan et al., 2018). Henz-Gastal-Oliveria proposed a network containing 12 convolution layers to jointly optimize the CFA sampling pattern and demosaicking (Henz et al., 2018). Kokkinos-Lefkimiatis investigated jointly demosaicking and denoising by a 5-layer network in an iterative Majorization-Maximization process (Kokkinos & Lefkimiatis, 2018). Huang et al. designed a lightweight CNN with dense connections and aggregated residual transformations for jointly demosaicking and denoising (Huang et al., 2018). Except the joint CFA design and demosaicking work (Henz et al., 2018), these CNN-based techniques focus on Bayer pattern CFA demosaicking and treat the RGB channels equally. However, compared to the red and blue channels, the green channel is sampled more densely in Bayer CFA images, and hence the green channel reconstruction is easier. This fact is exploited in the two-phase CNN (Tan et al., 2017), in which the green channel is recovered first and then used to guide the subsequent recovery of the other channels. This scheme is extended by Cui-Jin-Steinbach to a three-stage CNN, obtaining state of the art demosaicking accuracy (Cui et al., 2018).

Existing demosaicking CNNs are sequential and generally have more than 10 convolution layers. Moreover, recent demosaicking CNNs reported on arXiv tend to have more than 20 sequential layers. The CNN depth and width are both important for demosaicking accuracy (Henz et al., 2018). However, increasing the depth or width will also increase the training and demosaicking time: long offline training causes difficulty to hyper-parameter selection, and long online demosaicking causes latency. To speed up, we parallelize the reconstruction of the three channels by three CNNs. The training thus requires three GPUs, which are affordable today. At the online application end, the Field Programmable Gates Arrays (FPGA) implementation in the camera Digital Signal Processing units prefer parallel demosaicking to sequential processing.

Naively training one CNN for each channel would severely discard the cross-channel correlation, and hence foregoes the demosaicking accuracy. To attain both accu-

racy and efficiency, our solution is to recover the green-red and green-blue color difference planes instead of the red and blue channels. This draws inspiration from the color difference restoration strategy of the HA algorithm (Hamilton Jr. & Adams, 1997), which outperforms many demosaicking methods that hinge on sophisticated edge detection, in terms of both accuracy and speed (Niu et al., 2019). Moreover, the color difference planes are generally smoother than the corresponding color channels, thereby can be encoded with less parameters. We will show that, such an architecture achieves demosaicking accuracy comparable to state-of-the-art, while remarkably reducing the demosaicking time cost.

2. Overall Work-Flow

Many CNN-based demosaicking methods initialize the inputs by a fast interpolation scheme (e.g., (Tan et al., 2017); (Tan et al., 2018)). The initialization predicts the missing values at low cost, with acceptable accuracy in flat image regions, thereby easing the computational burden on the CNNs. In general, bilinear interpolation is a fast and versatile initialization tool for any CFA pattern. Particularly for Bayer CFA, our empirical study shows that Malvar-He-Cutler’s High Quality Linear Interpolation (HQLI) algorithm (Malvar et al., 2004), which is also linear and fast, is preferable to the bilinear interpolation for initializing the CNN input.

We define a Bayer CFA sampled image patch by M ; Its original red, green and blue channels by r , g and b . Notations \mathcal{R} , \mathcal{G} and \mathcal{B} are the sets of pixels whose red, green and blue components are originally available. In essence, HQLI enhances the bilinear reconstruction of one channel by the details (Laplacians) of another channel. Still, it suffers the “false color” and “zippering” artifacts around edges and textures. These aliasing problems are to be addressed by the subsequent CNN, which seeks for a mapping function f from the HQLI initialization $[r_0, g_0, b_0]$ to the true image $[r, g, b]$. Noticing that the network depth is a key factor for demosaicking performance, state of the art demosaicking CNNs generally have more than 10 layers. Each layer typically contains 128 or 64 filters of size $3 \times 3 \times 128$ or $3 \times 3 \times 64$. Their training and demosaicking time might be long. According to (Gharbi et al., 2016), it takes 2-3 weeks to train the lightweight (559,776 trainable parameters) CNN by Gharbi et al. using a modern GPU.

To speed up, we decouple the RGB demosaicking to restoring the green channel, the green-red difference plane and the green-blue difference plane. Particularly for parallel demosaicking, the color difference planes embed cross-channel correlation into the CNNs. Thus the task is to train

functions f_{gr} , f_g and f_{gb} , such that

$$\begin{aligned} f_{gr} : [\mathbf{g}_0 - \mathbf{r}_0, \mathbf{g}_0, \mathbf{b}_0] &\mapsto \mathbf{g} - \mathbf{r}, \\ f_g : [\mathbf{r}_0, \mathbf{g}_0, \mathbf{b}_0] &\mapsto \mathbf{g}, \\ f_{gb} : [\mathbf{r}_0, \mathbf{g}_0, \mathbf{g}_0 - \mathbf{b}_0] &\mapsto \mathbf{g} - \mathbf{b}. \end{aligned}$$

Here the left hand side of symbol \mapsto is the input, and the right hand side is the ideal output. In empirical study, we observe that \mathbf{b}_0 shows trivial contribution to the demosaicking performance of f_{gr} , and so does \mathbf{r}_0 to f_{gb} . Furthermore, we employ the residual network (He et al., 2016). Thus the mapping functions we seek for are

$$\begin{aligned} f_{gr} : [\mathbf{g}_0 - \mathbf{r}_0, \mathbf{g}_0] &\mapsto (\mathbf{g} - \mathbf{r}) - (\mathbf{g}_0 - \mathbf{r}_0), \\ f_g : [\mathbf{r}_0, \mathbf{g}_0, \mathbf{b}_0] &\mapsto \mathbf{g} - \mathbf{g}_0, \\ f_{gb} : [\mathbf{g}_0, \mathbf{g}_0 - \mathbf{b}_0] &\mapsto (\mathbf{g} - \mathbf{b}) - (\mathbf{g}_0 - \mathbf{b}_0). \end{aligned}$$

Fig. 2 depicts the overall work-flow of the proposed method.

3. Three-Stream Lightweight Networks

3.1. Network Design

We denote the CNN parameters for f_{gr} , f_g and f_{gb} by Θ_{gr} , Θ_g and Θ_{gb} respectively, to be learned from the training input-label patch pairs.

3.1.1. GREEN CHANNEL DEMOSAICKING CNN

As described in Section 2, f_g takes $[\mathbf{r}_0, \mathbf{g}_0, \mathbf{b}_0]$ as input. In particular, we define tensor

$$\mathbf{X}_{i,g} = [\mathbf{r}_0, \mathbf{g}_0, \mathbf{b}_0]_i$$

as the i th training observation, and tensor

$$\mathbf{Y}_{i,g} = [\mathbf{g} - \mathbf{g}_0]_i$$

as the associated label. The desirable Θ_g should have the prediction $f_g(\mathbf{X}_{i,g}; \Theta_g)$ very close to $\mathbf{Y}_{i,g}$. Accordingly, we define the loss function by the Mean Squared Error (MSE) between the predictions and the labels

$$e_g = \frac{1}{P} \sum_{i=1}^P \|f_g(\mathbf{X}_{i,g}; \Theta_g) - \mathbf{Y}_{i,g}\|_2^2. \quad (1)$$

Here P stands for the number of training observations.

The input block has a convolution layer, containing 64 filters of spatial support 3×3 and length 3 (in the feature dimension), followed by a Rectified Linear Unit (ReLU) layer. The subsequent 16 hidden layer-blocks have equal structure: each block includes Convolution, Batch Normalization (Ioffe & Szegedy, 2015) and ReLU layers; and each convolution layer contains 64 filters of spatial support 3×3

and length 64. Naturally, the prediction layer (right before the loss layer) has 1 filter of size $3 \times 3 \times 64$ to match the size of \mathbf{Y} . Table 1 outlines the number and size of the convolution filters involved in $f_g(\quad; \Theta_g)$. To keep the spatial resolution invariant, we pad one-pixel wide zeros at convolution boundaries along the spatial dimensions. We test exchanging the order of ReLU and Batch Normalization in the hidden blocks. Empirically, it is observed that performing Batch Normalization before ReLU yields slightly superior accuracy.

Note that our model estimates not only $\mathbf{g}(\mathcal{R})$ and $\mathbf{g}(\mathcal{B})$, but also $\mathbf{g}(\mathcal{G})$, which are originally available in the CFA images. Hence it may seem unnecessary for a CNN to spend time on restoring $\mathbf{g}(\mathcal{G})$. To test this speculation, we tried a CNN structure with the same hidden layers as Table 1, but takes tensor

$$[\mathbf{g}_0(\mathcal{G}_1), \mathbf{g}_0(\mathcal{G}_2), \mathbf{g}_0(\mathcal{R}), \mathbf{g}_0(\mathcal{B}), \mathbf{b}_0(\mathcal{G}_1), \mathbf{b}_0(\mathcal{G}_2), \mathbf{b}_0(\mathcal{R}), \mathbf{b}_0(\mathcal{B}), \mathbf{r}_0(\mathcal{G}_1), \mathbf{r}_0(\mathcal{G}_2), \mathbf{r}_0(\mathcal{R}), \mathbf{r}_0(\mathcal{B})]_i$$

as the input, and tensor

$$[(\mathbf{g} - \mathbf{g}_0)(\mathcal{G}_1), (\mathbf{g} - \mathbf{g}_0)(\mathcal{G}_2)]_i$$

as the label, where $\mathcal{G}_1 \in \mathcal{G}$ collects the pixel positions at odd rows; $\mathcal{G}_2 \in \mathcal{G}$ collects the pixel positions at even rows. Therefore this testing CNN only estimates $\mathbf{g}(\mathcal{R})$ and $\mathbf{g}(\mathcal{B})$. With identical experimental settings (except for the smaller training-label patch size), we observe that the experimental CNN performs demosaicking at faster speed but lower accuracy. This is probably because predicting $\mathbf{g}(\mathcal{G})$ acts similarly to an auto encoder-decoder mechanism, which extracts the underlying structure by reconstructing the inputs.

3.1.2. COLOR DIFFERENCE RECONSTRUCTION CNNS

The CNNs for $f_{gr}(\quad; \Theta_{gr})$ and $f_{gb}(\quad; \Theta_{gb})$ take the tensors

$$\begin{aligned} \mathbf{X}_{i,gr} &= [\mathbf{g}_0 - \mathbf{r}_0, \mathbf{g}_0]_i \\ \mathbf{X}_{i,gb} &= [\mathbf{g}_0 - \mathbf{b}_0, \mathbf{g}_0]_i \end{aligned}$$

as the i th input respectively. Their respective label tensors are

$$\begin{aligned} \mathbf{Y}_{i,gr} &= [(\mathbf{g} - \mathbf{r}) - (\mathbf{g}_0 - \mathbf{r}_0)]_i \\ \mathbf{Y}_{i,gb} &= [(\mathbf{g} - \mathbf{b}) - (\mathbf{g}_0 - \mathbf{b}_0)]_i. \end{aligned}$$

At image details, the estimated color components are highly likely to mismatch the captured color components, and hence the cross-channel difference is outlier-prone. For robustness to outliers, we adopt the L_1 -norm distance penalty function for the objective functional of Θ_{gr} ,

$$e_{gr} = \frac{1}{P} \sum_{i=1}^P |f_{gr}(\mathbf{X}_{i,gr}; \Theta_{gr}) - \mathbf{Y}_{i,gr}|_1, \quad (2)$$

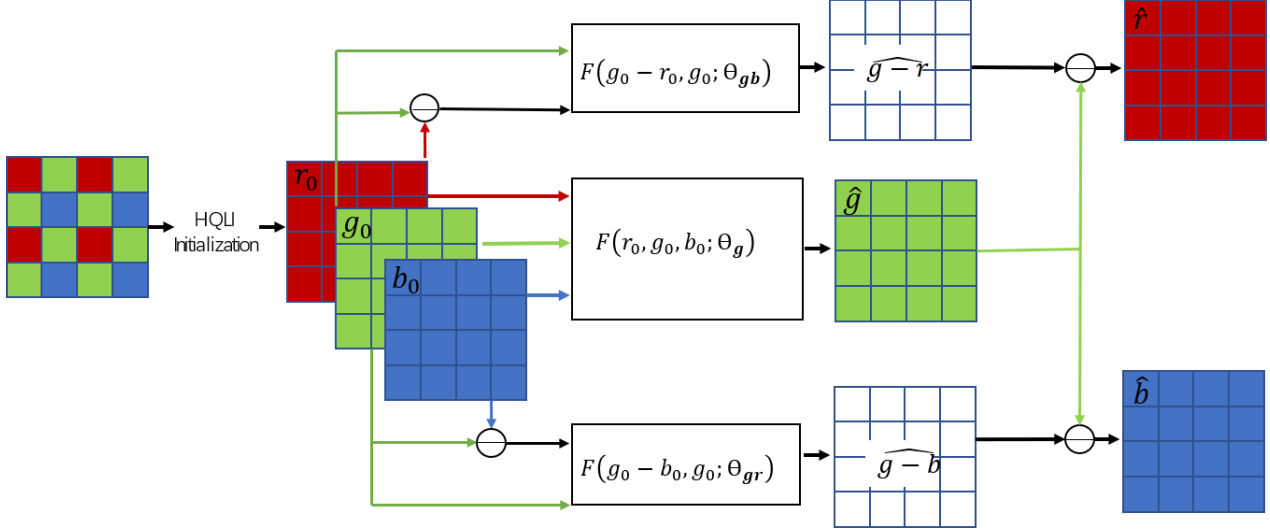


Figure 2. The overall work-flow of the proposed CNN-based demosaicking process.

layer index	num. of filters	feature dimension	spatial support
input	64	3	3×3
hidden 1	64	64	3×3
\vdots	\vdots	\vdots	\vdots
hidden 16	64	64	3×3
prediction	1	64	3×3

 Table 1. The number and size of the convolution filters involved in the CNN for $f_g(\cdot; \Theta_g)$.

and similarly for Θ_{gb}

$$e_{gb} = \frac{1}{P} \sum_{i=1}^P |f_{gb}(\mathbf{X}_{i,gb}; \Theta_{gb}) - \mathbf{Y}_{i,gb}|_1, \quad (3)$$

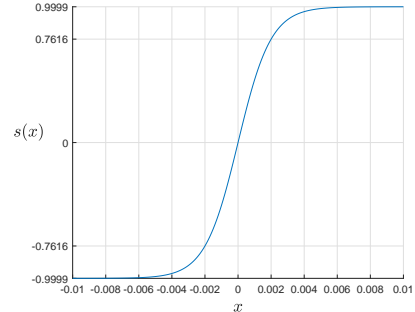
We then seek for Θ_{gr} that minimizes e_{gr} and Θ_{gb} that minimizes e_{gb} by CNN training.

It is known that the derivative of the absolute function $|x|$ in the L_1 -norm distance is not defined at $x = 0$. However, in practice, it is usually implemented as the sign function. Thus a small distortion may cause the derivative to jump to the opposite side. For robustness of back-propagation, we use the smooth logistic function

$$l(x) = \frac{2}{1 + e^{-kx}} - 1, \quad (4)$$

where k is set to 1000, to approximate the derivative of $|x|$. Fig.3 depicts the function curve of $l(x)$.

The CNNs for $f_{gr}(\cdot; \Theta_{gr})$ and $f_{gb}(\cdot; \Theta_{gb})$ share the same structure. Although the green-red and green-blue planes are easier to reconstruct than the red and blue channels, they are still harder to reconstruct than the green channel, due to the sampling frequency. This means that the


 Figure 3. The logistic function $l(x)$ we use in back propagation to approximate the sign function, which is usually used as the derivative of the absolute function $|x|$.

CNNs for $f_{gr}(\cdot; \Theta_{gr})$ and $f_{gb}(\cdot; \Theta_{gb})$ should be deeper or wider than $f_g(\cdot; \Theta_g)$. Here we adopt a wide but shallow structure, which has 6 hidden layers. Compared to a CNN of 20 hidden layers with the same number of trainable parameters, the wide CNN obtains similar accuracy at much faster demosaicking speed, as less Batch Normalizations are involved. The input layer convolves the input tensor with 256 filters of spatial support 3×3 and length 3.

The number of feature channels are narrowed down gradually in the subsequent 6 hidden layers, as shown in Table 2. Each hidden convolutional layer is followed by Batch Normalization and then ReLU. The prediction layer has 1 filter of length 64 and spatial support 7×7 , which is wider than its green channel CNN counterpart. This is because the red and blue channels are sampled more sparsely, so we increase the receptive field to include more original samples into the recovery.

3.2. Offline Training and Online Demosaicking

We choose the Waterloo Exploration Dataset (WED) dataset (Ma et al., 2017), which contains 4744 images, for training and validation. We randomly shuffle the order of the images in each dataset, and then partition each image to 50×50 patches. Patches from the first 95% images are used for training, we then discard the next 1792 consecutive patches, and use the rest patches for validation. This ensures that the training and validation patches are from different images, thus no validation patch nearly duplicates a training patch. Each training batch contains 128 input-label pairs.

The cost functions e_g , e_{gr} and e_{gb} are minimized by the Adaptive Moment Estimation (ADAM) optimizer (Kingma & Ba, 2015) independently, with the same hyper-parameter settings. The initial learning rate is set to 0.005, and is then halved every 5 epochs until reaching $\frac{0.005}{64}$. At the end of 50 training epochs, the models $\tilde{\Theta}_g$, $\tilde{\Theta}_{gr}$ and $\tilde{\Theta}_{gb}$ that yield the least validation error is used for online demosaicking. On our Nvidia 1070 GPU, each training epoch for either f_g , f_{gr} or f_{gb} takes about 55 minutes. $\tilde{\Theta}_g$ has 592,128 parameters, taking 6400kB memory; $\tilde{\Theta}_{gr}$ or $\tilde{\Theta}_{gb}$ has 745,024 parameters, taking 8100kB memory.

\mathbf{g} , $\mathbf{g} - \mathbf{r}$ and $\mathbf{g} - \mathbf{b}$ of a mosaicked image \mathbf{M} are finally estimated by:

$$\begin{aligned}\hat{\mathbf{g}} &= f_g([\mathbf{r}_0, \mathbf{g}_0, \mathbf{b}_0]; \tilde{\Theta}_g) + \mathbf{g}_0 \\ \widehat{\mathbf{g} - \mathbf{r}} &= f_{gr}([\mathbf{g}_0 - \mathbf{r}_0, \mathbf{g}_0]; \tilde{\Theta}_{gr}) + \mathbf{g}_0 - \mathbf{r}_0 \\ \widehat{\mathbf{g} - \mathbf{b}} &= f_{gb}([\mathbf{g}_0 - \mathbf{b}_0, \mathbf{g}_0]; \tilde{\Theta}_{gb}) + \mathbf{g}_0 - \mathbf{b}_0.\end{aligned}\quad (5)$$

This gives

$$\begin{aligned}\hat{\mathbf{g}}(\mathcal{G}) &= \mathbf{g}(\mathcal{G}) \\ \hat{\mathbf{r}}(\mathcal{R}) &= \mathbf{r}(\mathcal{R}) \quad \hat{\mathbf{r}}(\mathcal{G} \cup \mathcal{B}) = (\hat{\mathbf{g}} - \widehat{\mathbf{g} - \mathbf{r}})(\mathcal{G} \cup \mathcal{B}) \\ \hat{\mathbf{b}}(\mathcal{B}) &= \mathbf{b}(\mathcal{B}) \quad \hat{\mathbf{b}}(\mathcal{G} \cup \mathcal{R}) = (\hat{\mathbf{g}} - \widehat{\mathbf{g} - \mathbf{b}})(\mathcal{G} \cup \mathcal{R}),\end{aligned}$$

Note that some estimated values may be out of the range [0, 255]. They are further clipped to 0 or 255.

4. Experimental Results

Our offline training and online demosaicking are carried out on a Nvidia 1070 GPU with 8GB memory and an Intel i7-8700 CPU clocked at 3.2GHz with 6 cores (12 threads) and 32GB RAM. The implementation is conducted using the MatConvNet toolbox (Vedaldi & Lenc, 2015) in Matlab.

We evaluate the proposed Parallel CNN Demosaicking (PAD) on benchmark datasets McM (Zhang et al., 2011) and Kodak (Eastman Kodak Company). Table 3 compares the Peak Signal to Noise Ratio (PSNR) of our method with the state-of-the-art demosaicking CNNs, including Joint Denoising and Demosaicking (+Denoise) (Gharbi et al., 2016), Two-Stage Demosaicking (2-Stage) (Tan et al., 2017), Multiple CNNs for Demosaicking (Multiple) (Tan et al., 2018), Joint CFA Design and Demosaicking (+Design) (Henz et al., 2018), Three-Stage Demosaicking (3-Stage) (Cui et al., 2018), Cascaded Denoising and Demosaicking (Cascade) (Kokkinos & Lefkimiatis, 2018), Lightweight Denoising and Demosaicking (Light) (Huang et al., 2018). Following the PSNR measurement convention (e.g., (Tan et al., 2017)(Cui et al., 2018)), we exclude the 10 pixel wide image boundaries from the error statistics. In this comparison, the demosaicking accuracy of our method on the Kodak dataset is on a par with the Light CNN, 0.2dB higher than the 3-stage sequential CNN, and 0.56-1.40 dB higher than the other competing CNNs. The significantly superior accuracy verifies that our strategy effectively learns the inter-channel correlation. On the McM dataset, the PSNR of our model is 0.3dB lower than method Cascade and slightly lower (0.1dB) than methods +Denoise and +Design, but is still evidently higher than methods Multiple, 2-Stage and Light.

Our method is implemented in the same platform as the 2-stage and 3-stage methods, which exploit the cross-channel correlation in a sequential fashion. To investigate the effectiveness of parallel demosaicking, we compare our method with these two works in terms of PSNR for each channel, Structural Similarity (SSIM) measure (Wang et al., 2004), and demosaicking time (using CPU), by running their released source code on Kodak and McM. Table 4 lists their average accuracy and median speed (in seconds) evaluated on each test dataset. The time cost of the proposed PAD is between competing methods 2-Stage and 3-Stage, but it achieves noticeably higher PSNR and SSIM accuracy on Kodak, and performance on a par with 3-Stage on McM.

Table 3 also compares the proposed PAD to naively parallelizing the CNNs for R\G\B (termed as Direct), while the network architecture and experimental settings remaining identical. Without the cross-channel regularization, the parallel networks have accuracy inferior to method 3-stage and PAD, especially in the red and blue channels.

layer index	num. of filters	feature dimension	spatial support
input	256	2	3×3
hidden 1	128	256	3×3
hidden 2	128	128	3×3
hidden 3	128	128	3×3
hidden 4	64	128	3×3
hidden 5	64	64	3×3
hidden 6	64	64	3×3
prediction	1	64	7×7

Table 2. The number and size of the filters involved in the CNN for $f_{gr}(\cdot; \Theta_{gr})$ and $f_{gb}(\cdot; \Theta_{gb})$.

	Kodak	McM
+Denoise (Gharbi et al., 2016)	41.20	39.50
Cascade (Kokkinos & Lefkimiatis, 2018)	41.50	39.70
+Design (Henz et al., 2018)	41.86	39.51
Multiple (Tan et al., 2018)	42.04	37.62
2-Stage (Tan et al., 2018)	42.04	38.98
3-Stage (Cui et al., 2018)	42.39	39.39
Light (Huang et al., 2018)	42.60	39.21
Proposed	42.60	39.39

Table 3. Demosaicking accuracy measured by PSNR of the proposed method and state of the art CNN based demosaicking methods. Bold numbers highlight best performance in each column.

Fig. 4 demonstrates the visual performance of PAD by an example taken from Kodak. In the fine scale texture area close to the camera, the 2-Stage CNN suffers obviously severer false color artifacts than the 3-Stage CNN and the proposed PAD. In the coarse scale texture area further away from the camera, PAD visually performs the best.

5. Conclusion

In this paper, we have presented a parallel CNN-based framework for demosaicking. Initialized by the fast linear HQLI interpolation, our demosaicking system is integrated with cross-channel regularization by learning the underlying structure of the color difference planes. We have analyzed the auto encoder-decoder nature of our green channel demosaicking CNN. Furthermore, by approximating the derivative of absolute function by a smooth logistic function, our absolute error based objective functions are optimized more robustly during the back propagation process. Experimental results have verified the superiority of restoring the color difference planes to restoring the color channel directly. Moreover, comparison studies have also shown that the proposed parallel framework achieves the accuracy of top-performing sequential CNNs, while being significantly faster.

References

Buades, A., Coll, B., Morel, J.-M., and Sbert, C. Self-similarity driven color demosaicking. *IEEE Transactions on Image Processing*, 18(6):1192–1202, 2009.

Chung, K.-H. and Chan, Y.-H. Color demosaicing using variance of color differences. *IEEE Transactions on Image Processing*, 15(10):2944–2955, 2006.

Condat, L. and Mosaddegh, S. Joint demosaicking and denoising by total variation minimization. In *IEEE International Conference on Image Processing*, pp. 2781–2784, 2012.

Cui, K., Jin, Z., and Steinbach, E. Color image demosaicking using a 3-stage convolutional neural network structure. In *IEEE International Conference on Image Processing*, pp. 2177–2181, 2018.

Duran, J. and Buades, A. Self-similarity and spectral correlation adaptive algorithm for color demosaicking. *IEEE transactions on image processing*, 23(9):4031–4040, 2014.

Eastman Kodak Company. Low resolution kodak image dataset. <http://r0k.us/graphics/kodak/>, 1991.

Getreuer, P. Image demosaicking with contour stencils. *Image Processing OnLine*, 2:22–34, 2012.

	Kodak						McM					
	PSNR				SSIM	TIME	PSNR				SSIM	TIME
	R	G	B	RGB			secs	R	G	B	RGB	secs
2-Stage	41.38	44.85	41.04	42.04	0.974	5.10	39.14	42.10	37.31	38.98	0.963	1.78
Direct	41.54	45.61	40.86	42.16	0.987	-	39.24	42.78	37.49	39.21	0.980	-
3-Stage	42.07	45.18	41.09	42.39	0.989	12.20	39.60	42.60	37.68	39.39	0.980	7.06
Proposed	42.26	45.61	41.24	42.60	0.993	10.35	39.57	42.78	37.65	39.39	0.980	3.37

Table 4. Demosaicking accuracy measured by PSNR (for each channel and for the color image) and SSIM of the proposed method and state of the art CNN based demosaicking methods. Bold numbers highlight the best performance in each column.



Figure 4. Visual performance example on the 24th test image of Kodak.

Gharbi, M., Chaurasia, G., Paris, S., and Durand, F. Deep joint demosaicking and denoising. *ACM Transactions on Graphics*, 35(6):191, 2016.

Hamilton Jr., J. F. and Adams, J. E. Adaptive color plane interpolation in single sensor color electronic camera, 1997. [US Patent 5,629,734].

He, K., Zhang, X., Ren, S., and Sun, J. Deep residual learning for image recognition. In *IEEE CVPR*, pp. 770–778, 2016.

Henz, B., Gastal, E. S. L., and Oliveira, M. M. Deep joint design of color filter arrays and demosaicing. *Eurographics*, 37(2):389–399, 2018.

Huang, T., Wu, F. F., Dong, W., Shi, G., and Li, X. Lightweight deep residue learning for joint color image demosaicking and denoising. In *International Conference on Pattern Recognition*, pp. 127–132, 2018.

Ioffe, S. and Szegedy, C. Batch normalization: Accelerating deep network training by reducing internal covariate shift. *arXiv preprint arXiv:1502.03167*, 2015.

Kiku, D., Monno, Y., Tanaka, M., and Okutomi, M. Residual interpolation for color image demosaicking. In *Proc. IEEE International Conference on Image Processing*, pp. 2304–2308, 2013.

Kiku, D., Monno, Y., Tanaka, M., and Okutomi, M. Beyond color difference: residual interpolation for color

image demosaicking. *IEEE Transactions on Image Processing*, 25(3):1288–1300, 2016.

Kingma, D. P. and Ba, J. Adam: A method for stochastic optimization. In *International Conference on Learning Representations*, volume 5, 2015.

Kokkinos, F. and Lefkimiatis, S. Deep image demosaicking using a cascade of convolutional residual denoising networks. In *European Conference on Computer Vision*, 2018.

Li, X. Demosaicing by successive approximation. *IEEE Transactions on Image Processing*, 14(3):370–379, 2005.

Lu, Y. M., Karzand, M., and Vetterli, M. Demosaicing by alternating projections: theory and fast one-step implementation. *IEEE Transactions on Image Processing*, 19(8):2085–2098, 2010.

Ma, K., Duanmu, Z., Wu, Q., Wang, Z., Yong, H., Li, H., and Zhang, L. Waterloo Exploration Database: New challenges for image quality assessment models. *IEEE Transactions on Image Processing*, 26(2):1004–1016, 2017.

Malvar, H. S., He, L., and Cutler, R. High-quality linear interpolation for demosaicing of bayer-patterned color images. In *Proc. IEEE ICASSP*, pp. iii–485–8, 2004. [Matlab build-in function **demosaic()**].

Menon, D. and Calvagno, G. A regularization approach to demosaicing. In *Proc. of SPIE Visual Communications and Image Processing*, pp. 68221L, 2008.

Menon, D., Andriani, S., and Calvagno, G. Demosaicing with directional filtering and a posteriori decision. *IEEE Transactions on Image Processing*, 16(1):132–141, 2007.

Moghadam, A. A., Aghagolzadeh, M., Kumar, M., and Radha, H. Compressive demosaicing. In *IEEE International Workshop on Multimedia Signal Processing*, pp. 105–110, 2010.

Monno, Y., Kiku, D., Tanaka, M., and Okutomi, M. Adaptive residual interpolation for color image demosaicing. In *Proc. IEEE International Conference on Image Processing*, pp. 3861–3865, 2015.

Niu, Y., Ouyang, J., Zuo, W., and Wang, F. Low cost edge sensing for high quality demosaicing. *IEEE TIP*, 28(5), 2019.

Pekkucuksen, I. and Altunbasak, Y. Multiscale gradients-based color filter array interpolation. *IEEE Transactions on Image Processing*, 22(1):157–165, 2013.

Rossi, M. and Calvagno, G. Luminance driven sparse representation based demosaicing. In *IEEE International Conference on Image Processing*, pp. 1788–1792, 2014.

Su, C. Y. Highly effective iterative demosaicing using weighted-edge and color-difference interpolations. *IEEE Transactions on Consumer Electronics*, 52(2):639–645, 2006.

Szeliski, R. *Computer vision: algorithms and applications*. Springer Science; Business Media, 2010.

Tan, D. S., Chen, W.-Y., and Hua, K.-L. Deepdemosaicing: Adaptive image demosaicing via multiple deep fully convolutional networks. *IEEE Transactions on Image Processing*, 27(5):2408–2419, 2018.

Tan, R., Zhang, K., Zuo, W., and Zhang, L. Color image demosaicing via deep residual learning. In *2017 IEEE International Conference on Multimedia and Expo*, pp. 793–798, 2017.

Tsai, C.-Y. and Song, K.-T. Heterogeneity-projection hard-decision color interpolation using spectral-spatial correlation. *IEEE Transactions on Image Processing*, 16(1):78–91, 2007.

Vedaldi, A. and Lenc, K. Matconvnet – convolutional neural networks for matlab. In *ACM Int. Conf. on Multimedia*, 2015.

Wang, Y.-Q. A multilayer neural network for image demosaicing. *IEEE ICIP*, pp. 1852–1856, 2014.

Wang, Z., Bovik, A. C., Sheikh, H. R., and Simoncelli, E. P. Image quality assessment: from error visibility to structural similarity. *IEEE Transactions on Image Processing*, 13(4):600–612, 2004.

Wu, J., Timofte, R., and Gool, L. V. Demosaicing based on directional difference regression and efficient regression priors. *IEEE Transactions on Image Processing*, 25(8):3862–3874., 2016.

Wu, X. and Zhang, N. Primary-consistent soft-decision color demosaicing for digital cameras. *IEEE Transactions on Image Processing*, 13(9):1263–1274, 2004.

Zhang, L., Wu, X., Buades, A., and Li, X. Color demosaicing by local directional interpolation and nonlocal adaptive thresholding. *Journal of Electronic Imaging*, 20(2):023016, 2011.